How to cite: Angew. Chem. Int. Ed. 2025, e202425535
doi.org/10.1002/anie.202425535

Batteries Hot Paper

Anion Adsorption at the Inner-Helmholtz Plane Directs Cathode Electrolyte Interphase Formation

Yuchen Ji[+], Yuxiang Huang[+], Zihang Dong, Jianjun Fang, Peng Liu, Shiqi Liu, Aimin Cao, Haoyu Xue, Shiming Chen, Jimin Qiu, Peng-Hu Du, Kunchen Xie, Shida Xue, Tao Shen, Guorui Zheng, Xiyao Zhao, Zu-Wei Yin, Kai Yang, Hai Lin, Kang Xu, Feng Pan,* and Luyi Yang**

Abstract: Constructing a stable cathode-electrolyte-interphase (CEI) on cathode surface constitutes the foundation of realizing high-voltage Li-ion batteries, yet its formation, a highly heterogeneous process involving irreversible reactions between electrolyte components and cathode materials, remains poorly understood. Herein, combining multiple in situ/operando interfacial characterization techniques, we establish the correlation between interfacial structure and interphasial chemistry, and reveal the key role played by adsorptive behavior of various electrolyte components in the inner-Helmholtz plane during CEI formation. Quartz crystal microbalance equipped with dissipation modification detects that difluorooxalatoborate ($DFOB^-$) anion preferentially adsorbed on $LiCoO_2$ tends to expel carbonate solvents from the adsorption layer, thus suppressing their electrochemical decomposition at high voltages and leading to a more compact CEI derived from anions with limited contribution from organic ingredients. Consequently, the CoO_2 lattice structure protected by the dense CEI remains intact despite near-complete delithiation, thereby ensuring excellent cycling stability for 4.7 V operation of $LiCoO_2$ cathode. The atomistic-level insight into the key factors that govern CEI formation provides directive knowledge that accelerates electrolyte design for high-voltage batteries.

Introduction

Raising the operating voltage of cathode materials is the most direct, economical and effective approach to increase the energy density of lithium-ion (LIBs) or lithium-metal batteries (LMBs).[1] Taking $LiCoO_2$ (LCO) as an example, as the cut-off voltage is raised from 4.2 V to 4.6 V vs Li/Li^+, the specific capacity sharply rises from 140 $mAh\,g^{-1}$ to 220 $mAh\,g^{-1}$, which corresponds to an additional >60 % specific energy.[2] However, the conventional carbonate-based electrolytes generally cannot support LCO to operate at such high potentials because they cannot form a cathode-electrolyte interphase (CEI) that effectively prevents the irreversible reactions between the electrolytes and the cathode surface.[2d,3] As a result, state-of-the-art LIBs only utilize less than half of the Li^+-storage in LCO by limiting its operating potential under 4.1 V, otherwise the LIBs degrade rapidly or even ends catastrophically, due to sustained consumption of the electrolytes,[4] transition metal dissolution[5], release of lattice oxygen,[6] as well as detrimental phase transition.[7]

In recent years, diversified electrolyte design strategies have been explored, including componential optimization,[8] additive engineering[5b,9] and super concentrating,[10] with the

[*] Y. Ji,[+] Y. Huang,[+] J. Fang, A. Cao, H. Xue, S. Chen, J. Qiu, K. Xie, S. Xue, H. Lin, F. Pan, L. Yang
School of Advanced Materials, Peking University Shenzhen Graduate School, Shenzhen, 518055, China
E-mail: panfeng@pkusz.edu.cn
yangly@pkusz.edu.cn

Z. Dong, X. Zhao
School of Environment and Energy, Peking University Shenzhen Graduate School, Shenzhen, 518055, China

P. Liu, T. Shen
Biolin Scientific AB, Hängpilsgatan 7, Västra Frölunda, SE-426 77, Sweden

S. Liu
Institute of Advanced Battery Materials and Devices, College of Materials Science and Engineering, Beijing University of Technology, Beijing 100124, China

P.-H. Du
School of Materials Science and Engineering, Peking University, Beijing 100871, China

G. Zheng
Institute of Materials Research (IMR), Tsinghua Shenzhen International Graduate School, Tsinghua University, Shenzhen 518055, China

Z.-W. Yin
College of Energy, Xiamen University, Xiamen 361005, China

K. Yang
Advanced Technology Institute, Department of Electrical and Electronic Engineering, University of Surrey, Guildford, Surrey, GU2 7XH, UK

K. Xu
SES AI Corp., Woburn, MA 01801, USA
E-mail: kang.xu@ses.ai

[+] These authors contributed equally to this work.

© 2025 Wiley-VCH GmbH

purpose to construct interphases that can accommodate the strongly oxidative surface of LCO at full delithiation.[11] Similar to solid-electrolyte-interphase (SEI) on the anode,[12] CEI consists of organic and inorganic species, but its formation process is much more complicated because the reaction involves not only the electrolyte components but also the cathode active materials (transition metal, oxygen layer and the structural transformation). Recent findings have shown that an organic-rich CEI is not only fragile against volume changes during repeated lithiation/delithiation, but also prone to further oxidation at high voltages; whereas an inorganic-rich CEI with high surface energy, mechanical strength and oxidative stability is more resistant against the oxidative cathode surface and hence more suitable for surface protection.[8d,13] Contrary to SEI formation where the solvation sheath structure of cations plays a major role,[14] CEI formation is more closely related to the anionic species in the electrolytes, due to the nature of the Coulombic interaction between the positively charged cathode surface and the negatively-charged anions.[15] Hence, how the anionic species adsorb in the inner-Helmholtz plane and how these anions eventually decompose should dictate the forthcoming CEI chemistry. Under this context, compared with the carbonate solvent molecules that usually prefer to be associated with cation (such as Li^+) but remain aloof toward anionic species (such as PF_6^-),[16] anions in an electrolyte are more likely to assemble at the inner-Helmholtz plane of the cathode surface, and their oxidative decomposition would lead to the inorganic-rich CEI if such oxidative decomposition could outcompete the solvent molecules. The effects of various salt anions on high-voltage performance have been reported,[8c,13a,17] showing varying degrees of success. However, these scattered reports, obscured by complex electrode-electrolyte interfacial processes, have not been able to reveal the underneath mechanism in a systematic and consistent manner how anion-cathode interaction directly affects the interfacial structures on cathode and the subsequent interphasial chemistry, and whether there exists a correlation between the transient interfacial structures and the CEI chemistry.

Herein, combining a series of in situ/operando interfacial probing techniques, we report a concerted approach that unveils the correlation between the anion-adsorption in inner-Helmholtz plane of cathode and the effectiveness of CEI thus formed that supports high-voltage LCO. With the aid of quartz crystal microbalance with dissipation mode (QCM–D), we first experimentally measured the adsorption behaviors of anions on LCO and compared their changes with the variation of anionic species. Exhibiting a higher adsorption energy on the LCO surface than that of PF_6^-, $DFOB^-$ tends to form a heavier and stiffer adsorption layer that more effectively shields carbonate solvent molecules from the inner-Helmholtz plane. The segregation of solvent molecules from LCO surface impedes their eventual electrochemical decomposition, hence minimizing their participation in CEI formation, which is directly proved via in situ attenuated total reflectance Fourier transform infrared (ATR-FTIR) spectroscopy and in situ confocal Raman spectroscopy. The new CEI chemistry, as monitored in situ by electrochemical quartz crystal microbalance with dissipation (EQCM–D), now consists of more inorganic ingredients from anion-decomposition, and successfully supports the cycling stability of LCO cathode at ultra-high potentials above 4.7 V with almost full delithiation, which has been predicted by Goodenough and co-workers in their original report on LCO[18] but was never realized due to the absence of qualified electrolytes and interphases. The newly accessible capacities at higher potential result in high cell-level volumetric energy density of ~560 $Wh\,L^{-1}$, with remarkable pouch cell performances at both high-temperature and high-rates.

Results and Discussion

Interfacial Adsorption Behaviors of Anions

According to scanning electron microscopy (SEM) image (Figure S1) and X-ray diffraction (XRD) patterns (Figure S2, Table S1), the LCO materials show well-defined morphologies around 5 μm and a typical layered phase. Carbonate-based electrolyte consisting of 1 M $LiPF_6$ dissolved in ethylene carbonate (EC) and ethylmethyl carbonate (EMC) at volumetric ratio of 3:7 serves as baseline electrolyte (hereafter denoted as SE). To construct an anion-derived CEI of varying chemistries, various amounts of lithium difluoro(oxalato)borate (LiDFOB) are introduced to replace the same moles of $LiPF_6$ so that the total concentration of Li^+ remains constant. Based on the long-term cycling (Figure S3) and rate capability (Figure S4) tests, the electrolyte containing an equimolar ratio of $LiPF_6$ and LiDFOB (i.e., 0.5 M $LiPF_6$ + 0.5 M LiDFOB) presents the most pronounced performance improvements under both conditions, which is therefore adopted for further studies (denoted as DE hereafter).

Due to the interaction between electrolyte and cathode surface, the components of the electrolyte adsorbed at the interface differ from those in the bulk, with the former playing a truly critical role to the formation of CEI.[19] However, understanding adsorption behavior remains a challenging topics in battery research, requiring innovative in situ/operando techniques. Quartz crystal microbalance with dissipation mode (QCM–D) has been used as a powerful tool to study the adsorption phenomena in the field of biological chemistry, environmental science, etc..[20] Herein, we applied such technique on electrolyte-LCO systems to study how these components in SE and DE adsorb on LCO.

The experimental set-up is represented in Figure 1a, where the Au chip was coated with LCO slurry and immersed in EC/EMC (vol% 3:7) solvent mixture that serves as the salt-free baseline. Overtones of 3, 5, and 7 are simultaneously monitored to verify the accuracy of model. As the frequency and dissipation stabilize (green region in Figure 1b–c and Figure S5), SE and DE are respectively injected into the chamber to replace the neat solvent mixture, which consequently causes significant frequency decrement in comparison with baseline (Figure 1b–c, Fig-

© 2025 Wiley-VCH GmbH

15213773, 0, Downloaded from https://onlinelibrary.wiley.com/doi/10.1002/anie.202425535 by University Town Of Shenzhen, Wiley Online Library on [17/03/2025]. See the Terms and Conditions (https://onlinelibrary.wiley.com/terms-and-conditions) on Wiley Online Library for rules of use; OA articles are governed by the applicable Creative Commons License

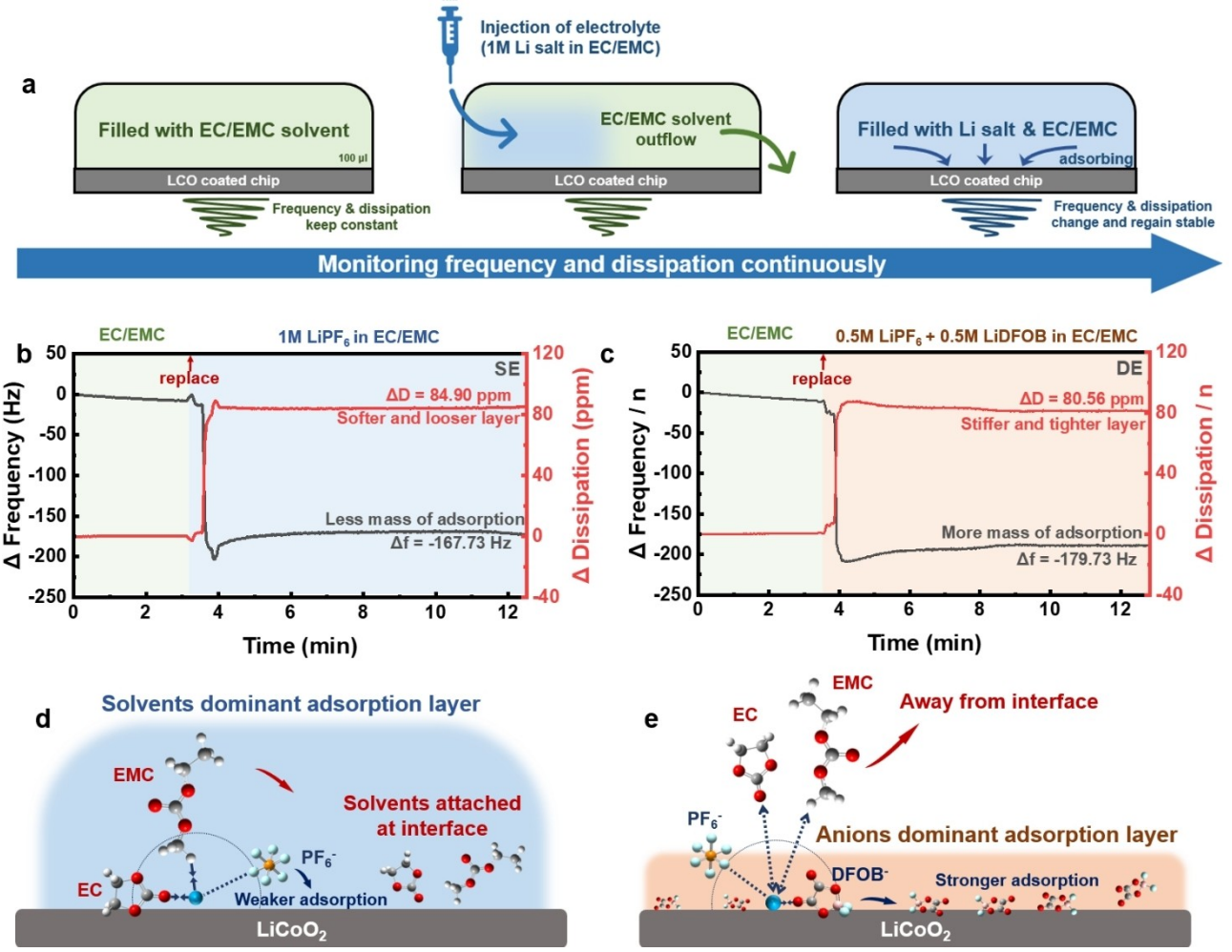

Figure 1. Adsorption behaviors and corresponding solvation variation at the LCO interface measured via QCM-D. (a) Schematic diagram of QCM–D set-up measuring the adsorption phenomenon. The variation of frequency and dissipation of LCO coated chip before and after replacing the EC/EMC solvent with SE (b) and DE ($n=7$) (c). Schematic illustration of adsorption and solvation variation at LCO interface in SE (d) and DE (e).

ure S5 and Table S2). It is worth mentioning here that if the original EC/EMC solvent mixture is replaced by the same solvent mixture, there is no frequency or dissipation variation after initial minor fluctuations (Figure S6), which verifies that mere liquid replacement does not cast sufficient influence on QCM–D signals in liquid environment. Thus, the frequency change of QCM–D can only be caused by the viscoelastic properties of liquid and the adsorbed mass.[21] To rule out the influence of the former, an oscillatory/dynamic mode viscoelastic measurement-similar to the operating mechanism of QCM–D-was used to analyze the electrolyte properties. The viscosity comparison between SE and DE shows that their values are identical (Figure S7). Therefore, larger decrement in frequency of DE than SE indicates a greater adsorption mass of components of electrolyte at the interface when controlling same sample preparation condition.[21–22] Larger adsorbing mass at interfacial in DE may be attributed to the stronger adsorption tendency of $DFOB^-$ comparing to the PF_6^-, which is also proven by density functional theory (DFT) calculations (Figure S8–S9 and Table S3).

Furthermore, by switching off the working voltage to the sensor periodically while monitoring the oscillation decay, dissipation (D) values can also be measured. Generally, a softer adsorption layer tends to be coupled with the surrounding medium, leading to a shorter decay time and a higher D, while a more rigid layer is less affected by the environment, as characterized with a lower D value.[23] What is interesting here is that, despite a stronger and larger mass of $DFOB^-$ adsorption on LCO, the corresponding ΔD across various overtones is lower than that observed with SE. Since SE and DE exhibit identical viscosity values, the different D values could be attributed to the fact that the $DFOB^-$ adsorption layer possesses mechanical properties with higher rigidity and a lower coupling tendency with the solution medium.

A series of spectral characterizations have been carried out with assistance from the density functional theory (DFT) calculation. In the Fourier transform infrared (FTIR)

© 2025 Wiley-VCH GmbH

15213773, 0, Downloaded from https://onlinelibrary.wiley.com/doi/10.1002/anie.202425535 by University Town Of Shenzhen, Wiley Online Library on [17/03/2025]. See the Terms and Conditions (https://onlinelibrary.wiley.com/terms-and-conditions) on Wiley Online Library for rules of use; OA articles are governed by the applicable Creative Commons License

spectra (Figure S10), the peaks at ~842 cm^{-1}, ~1200 cm^{-1}, ~1310 cm^{-1} and ~1720 cm^{-1} are indexed to the solvation of Li^+-EMC, and signals at ~730 cm^{-1} and ~1407 cm^{-1} to Li^+-EC. All these signals attenuate after the introduction of LiDFOB, indicating the weakened Li^+ solvation with carbonate solvent molecules. Similar trends are also observed in Raman spectra (Figure S11), where the solvation signals of Li^+-EC (~742 cm^{-1}, ~902 cm^{-1}, ~972 cm^{-1}, ~1088 cm^{-1}, ~1223 cm^{-1} and ~1777 cm^{-1}) and Li^+-EMC (~1486 cm^{-1}) weakens in DE, accompanied with the emergence of $DFOB^-$ and Li^+-$DFOB^-$ signals (~620 cm^{-1}). In addition to FTIR and Raman, ^{7}Li nuclear magnetic resonance (NMR) also indicate that $DFOB^-$ weakens Li^+-carbonate association, because ^{7}Li NMR signal experiences a downfield shift in presence of $DFOB^-$ (Figure S12a), suggesting that Li^+ nuclei are de-shielded from the electron cloud provided by carbonyl functionalities in carbonate molecules.[24] Moreover, the ^{19}F NMR signal corresponding to the interaction between Li^+ and PF_6^- (Figure S12b) reveal declined intensity in presence of $DFOB^-$, which may be attributed to the decreasing population of Li^+ in the direct vicinity of PF_6^-. Moreover, the downfield shift of peak positions also indicates the weakened interaction of Li^+ with PF_6^-.[24–25] These results reveal that the interaction between Li^+ and EC, EMC, and PF_6^- weakens with the introduction of the $DFOB^-$ anion. DFT results (Figure S13) also show that $DFOB^-$ possesses the highest coordinating strength with Li^+, thereby diminishing the interaction of EC, EMC and PF_6^- with Li^+, as illustrated in Figure S14.

Based on the QCM–D results, different interfacial adsorption models in SE and DE are proposed. In SE, Li^+ and PF_6^- are adsorbed to LCO along with the corresponding solvent molecules in the solvation structures (Figure 1d). Tighter coordination of EC and EMC solvents with Li^+ in SE suggests a higher likelihood of these molecules populating the inner-Helmholtz plane at LCO interface, forming a solvent-abundant adsorption layer. However, the solvents have relatively low affinity towards LCO surface while positively charged Li^+ repels LCO surface as well, leading to the lower adsorbing mass and a more diffusive adsorption layer. Such an adsorption layer tends to be more associated with the surrounding medium (solvent in electrolyte bulk), hence resulting in the higher ΔD. By contrast, $DFOB^-$ in DE (Figure 1e), thanks to its high adsorption energy on LCO, tends to be aggregated in the inner-Helmholtz plane and more tightly associated to the surface of LCO with higher mass. Considering that the presence of $DFOB^-$ significantly reduces Li^+-solvent interactions, it is likely that $DFOB^-$ dominates the inner-Helmholtz plane on LCO surface. Such an interfacial structure rich in anion-adsorption exhibits both higher mass and rigidity, and predicts the forthcoming interphasial chemistry once the potential of cathode crosses certain threshold for electrochemical oxidation.

Anion Adsorption Directed CEI Formation

To correlate the adsorption layer with the CEI formation process, in situ ATR-FTIR was further applied to LCO cathode coated on nickel foam (Figure S15), which can be infiltrated with electrolyte, thus the detected signals mainly arise from the electrolyte information near the surface of LCO. Before the measurement, the FTIR spectrum of electrolyte at the open circuit potential (OCP) was recorded as the baseline, so that the detected peaks during charging can be attributed to the oxidative decomposition of electrolyte components.

During the charging process, both SE and DE show reverse peaks of absorbance, which represent the consumption of relevant components (Figure S16). The selected potential points during the in situ ATR-FTIR can be indexed to the ex situ FTIR measurements (Figure 2a) as well as peak positions calculated by DFT simulations (Figure S10b). The negative peaks appearing during the charging process in SE mainly correspond to EC and EMC, directly proving the decomposition of both solvent molecules. In stark contrast, the peaks representing EMC are barely visible in DE during charging, indicating inhibited EMC decomposition. An extra peak appears at ~1045 cm^{-1} in DE, which was assigned to $DFOB^-$ according to DFT calculation (Figure S10b), directly verifying the participation of $DFOB^-$ in CEI formation. As the charging potential increases, the baseline shift upward can be attributed to the accumulation of interfacial species, further confirming the formation of the CEI.[26]

Since the FTIR characteristic peaks of EC are highly overlapping with $DFOB^-$ and Li^+-$DFOB^-$ as presented in Figure S10b, we further employed in situ confocal Raman to differentiate the interfacial evolution of EC from other components (Figure 2b). In both SE and DE two pronounced peaks located at ~892 and ~902 cm^{-1} were detected at OCP, which can be attributed to EC and Li^+-EC, respectively, according to ex situ Raman measurement (Figure S11a) and DFT calculations (Figure S11b). During charging, the free EC molecule peak disappears gradually, which can be attributed to the extraction of Li^+ from LCO lattice, which coordinates with EC at the LCO surface; upon discharging, Li^+-EC solvation peaks vanish at the low potential range accompanied with the reappearance of free EC signals in both electrolytes, owing to the Li^+-EC desolvation at the interface and the lithiation of LCO. Most importantly, it is noteworthy that at the high-voltage range (>4.5 V), the Li^+-EC solvation structure in SE also vanishes, which could be attributed to its continuous consumption on LCO at high potentials through electrochemical oxidation, which eventually leads to an organic-rich CEI chemistry. By contrast, the signal of Li^+-EC in DE remains nearly unchanged during the entire charging process, indicating the stabilization of electrolyte-LCO in presence of the CEI derived from $DFOB^-$ that effectively prevents EC decomposition.

DE and SE are expected to result in entirely different CEI chemistries and properties. Herein, EQCM–D again is used to monitor the real-time CEI evolution process during

© 2025 Wiley-VCH GmbH

15213773, 0, Downloaded from https://onlinelibrary.wiley.com/doi/10.1002/anie.202425535 by University Town Of Shenzhen, Wiley Online Library on [17/03/2025]. See the Terms and Conditions (https://onlinelibrary.wiley.com/terms-and-conditions) on Wiley Online Library for rules of use; OA articles are governed by the applicable Creative Commons License

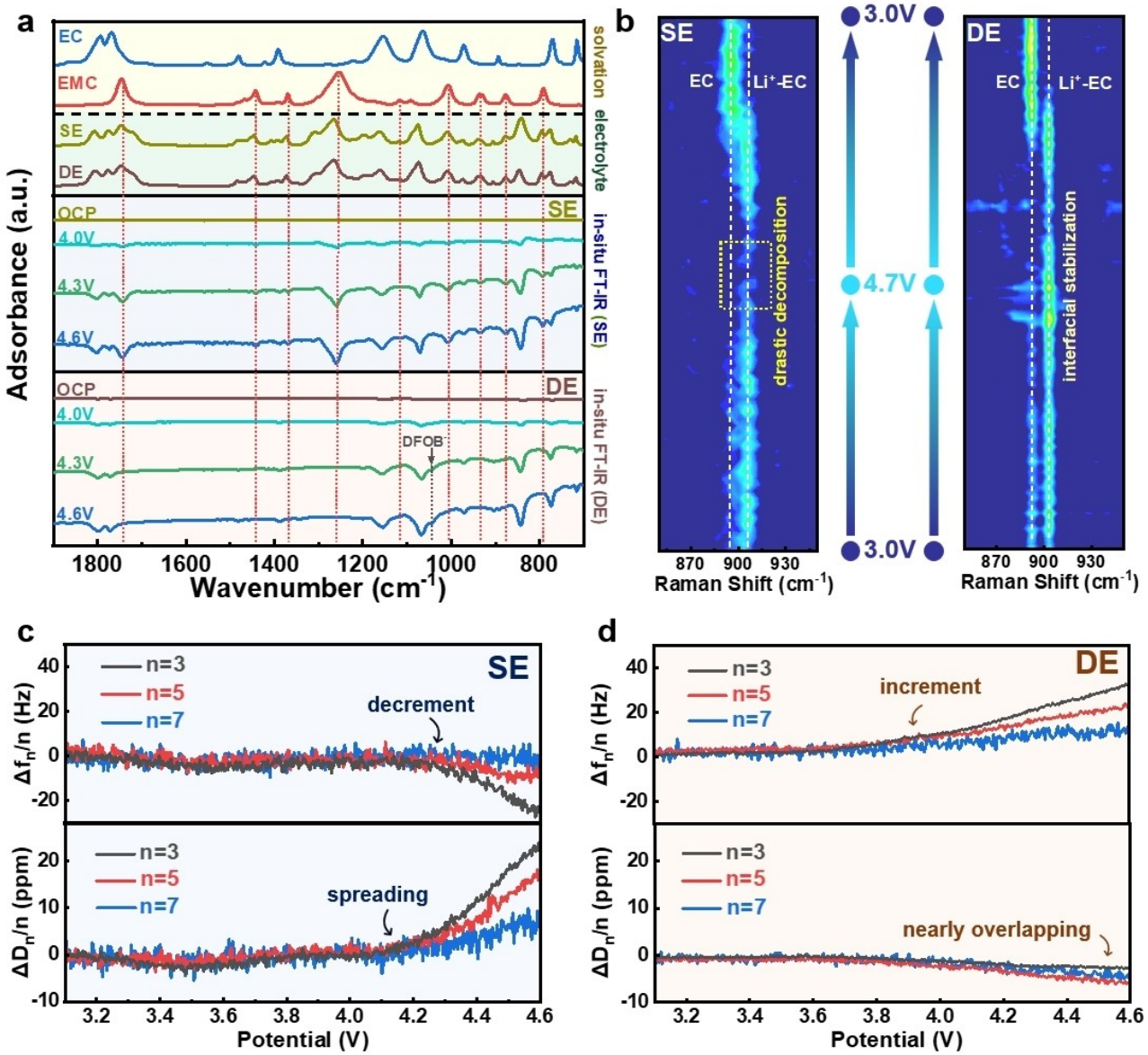

Figure 2. In situ probing of the interfacial evolution as the formation of CEI. (a) In situ FTIR signals in both electrolytes compared with bulk FTIR signals of solvents and electrolytes. (b) In situ Raman detection of the Raman signal variations of electrolytes at the LCO interface in SE and DE. Frequency and dissipation variation of LCO coated chip measured via EQCM–D during the charging process in SE (c) and DE (d).

charging (Figure 2c–d). For LCO during charging, its frequency variation is the coupled results of both de-lithiation (negative mass change) and CEI formation (positive mass change). The net mass increase (decrease in frequency) in SE is detected at ~4.1 V, which is in accordance with the decomposition potential of carbonate molecules.[3a] Thus, it can be inferred that a continuously growing CEI is formed on LCO, which overwhelms the mass decrease due to de-lithiation. In comparison, the mass variation of LCO electrode in DE shows a downward trend (increase in frequency) from ~3.9 V, which coincides with the initial delithiation potential of LCO, and outweighs the mass accumulation due to electrolyte decomposition and CEI formation. Apparently, the mass increases corresponding to CEI growth is now limited by the effectiveness of CEI in preventing sustained solvent decomposition. The striking contrast in the EQCM–D behaviors between SE and DE highlights the difference in CEI chemistries and their associated properties. This suggests the formation of a much heavier yet less protective CEI in SE, likely due to the sustained decomposition of EC and EMC (Figure 2a-b).

Apart from mass, the mechanical properties of different CEIs can be evaluated from their dissipative information. In SE, a drastic increase of D values is detected at ~4.1 V, accompanied by an obvious spreading of various overtones. On one hand, the increase of dissipation indicates the growth of a relatively soft (i.e. organic-rich) CEI;[27] on the other hand, as different harmonics detect different areas of

© 2025 Wiley-VCH GmbH

15213773, 0, Downloaded from https://onlinelibrary.wiley.com/doi/10.1002/anie.202425535 by University Town Of Shenzhen, Wiley Online Library on [17/03/2025]. See the Terms and Conditions (https://onlinelibrary.wiley.com/terms-and-conditions) on Wiley Online Library for rules of use; OA articles are governed by the applicable Creative Commons License

the electrode, the separation of dissipation between various overtones also indicates a non-uniform distribution of mass.[23a] Therefore, it can be speculated that a soft and unevenly distributed CEI is formed on LCO with a greater mass. Contrarily, in DE, the dissipation curves for three different harmonics exhibit decreasing tendencies, nearly overlapping during the charging process. This result indicates the formation of a relatively rigid or inorganic-rich CEI with homogeneous spatial distribution on the surface of LCO.

CEI Chemistry

The distinct difference in CEI morphologies can be visually verified by the cryo-TEM images of cycled LCO particles (Figure 3a and 3b), where a smooth and compact CEI layer

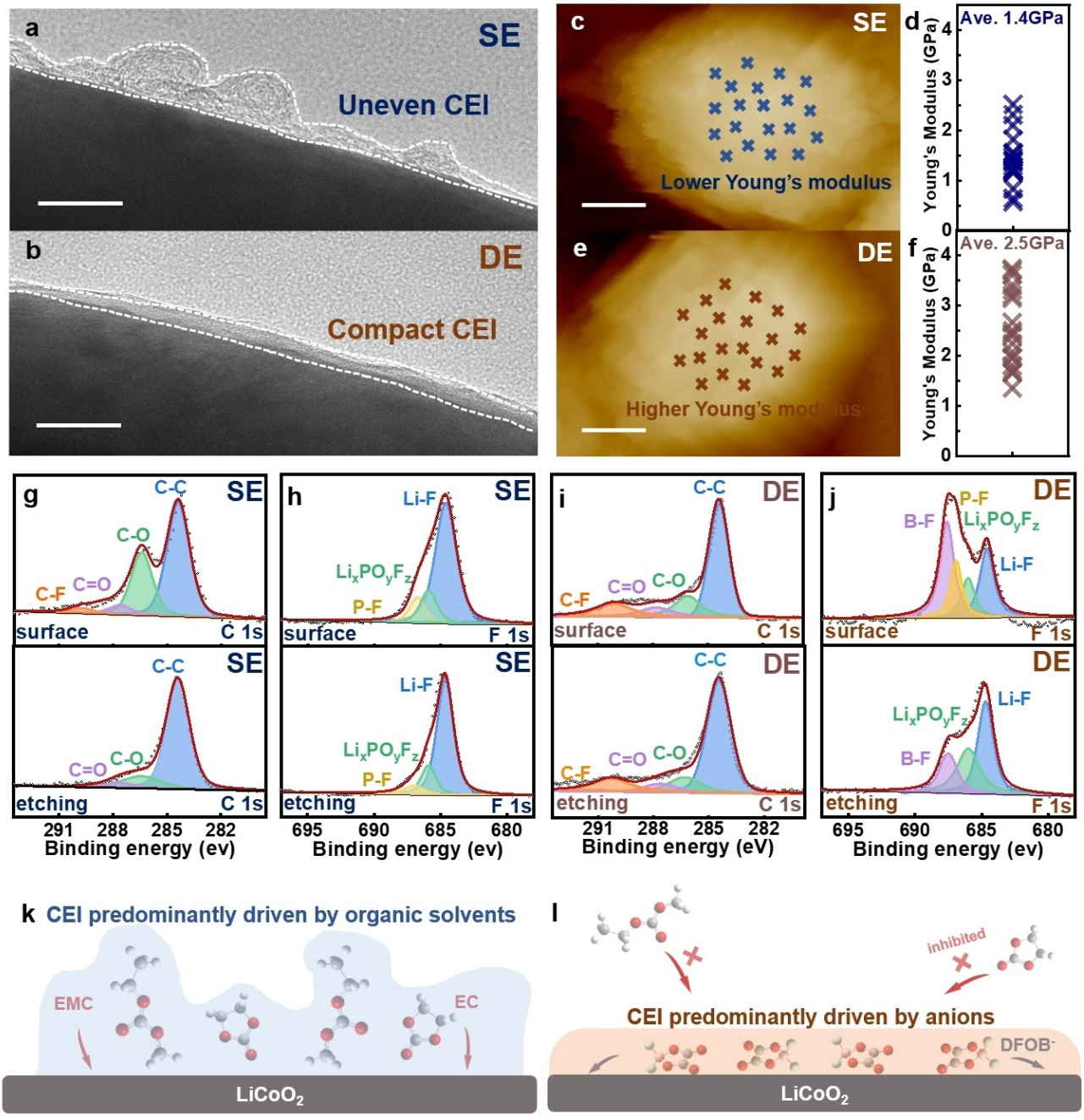

Figure 3. Characterizing the formation of CEI. Cryo-TEM image of the CEI formed on the surface of LCO particles cycled in SE (a) and DE (b), scale bar 20 nm. AFM morphological images of LCO surface cycled in SE (c) and DE (e), attached with the Young's modulus of LCO cycled in SE (d) and DE (f) corresponding to the selected 20 points in (c) and (e), respectively (scale bar: 1 μm). XPS spectra of cycled LCO electrode of C 1s in SE (g), F 1s in SE (h), C 1s in DE (i) and F 1s in DE (j). Schematic illustration of the CEI formed in SE (k) and DE (l).

© 2025 Wiley-VCH GmbH

15213773, 0, Downloaded from https://onlinelibrary.wiley.com/doi/10.1002/anie.202425535 by University Town Of Shenzhen, Wiley Online Library on [17/03/2025]. See the Terms and Conditions (https://onlinelibrary.wiley.com/terms-and-conditions) on Wiley Online Library for rules of use; OA articles are governed by the applicable Creative Commons License

is formed in DE, distributing evenly on the surface of LCO, whereas the CEI formed in SE shows irregular morphology and greater thickness. Atomic force microscope (AFM) of cycled LCO particles directly measures the Young's modulus of CEI, confirming that $DFOB^-$-originated CEI in DE is more rigid and mechanically strong (Figure 3c–f). The three-dimensional reconstruction images based on AFM reveal that LCO cycled in DE possesses a flatter surface than in SE (Figure S17). The uniform and robust CEI formed in DE not only better passivates the surface of LCO to suppress decomposition of solvent molecules, but also minimizes the local strain and layer slip in the near surface region, preventing the undesirable structural and phase transformation of LCO.

To correlate the enhanced mechanical properties of CEI with its chemical compositions, X-ray photoelectron spectroscopy (XPS) and time-of-flight secondary ion mass spectroscopy (TOF-SIMS) were combined to identify the chemical components in CEIs. Compared with DE-originated CEI, the SE-originated CEI exhibits obviously higher signals of C–O in C 1s XPS spectra at the upper surface (Figure 3g) than DE (Figure 3i), confirming an organic-rich CEI from SE contributed by the decomposition of solvent molecules, which are generally regarded as a chemically unstable and mechanically weak.[12] The F 1s XPS spectra detect an extra peak for DE-originated CEI attributed to B–F products (687.6 eV), which also exhibits higher intensity at the upper surface (Figure 3h and 3j), accompanied by peaks of B–O (191.3 eV) and B–F (193.3 eV) in B 1s spectra of DE (Figure S18). Corresponding TOF-SIMS signals including BO_2^- (Figure S19a) and BOF_2^- (Figure S19b), whose concentrations are also enriched at upper part of CEI (Figure S19c-d), further associate the CEI chemistry with the participation of $DFOB^-$. Comparison of the XPS results for the CEI after the initial cycle and following long-term cycling (Figure S20) also reveals that the CEI components formed in DE remained stable throughout cycling. In contrast, the CEI derived from SE deteriorated as cycling progressed, with the appearance of undesirable species, such as C–O and $Li_xPO_yF_z$, accumulating over time.

By calculating the frontier molecular orbitals, $DFOB^-$ anion exhibits relatively higher HOMO values compared to other components (Figure S21), making it more susceptible to oxidation. This preferential oxidation leads to the formation of a denser, boron-containing inorganic layer of CEI. This speculation is supported by the B–F and B–O bonds in XPS measurements (Figure 3j and Figure S18), as well as the detection of BO_2^- and BOF_2^- via TOF-SIMS (Figure S19). Additionally, XPS and TOF-SIMS reveal a vertical distribution pattern of boron-containing components, with B content intensity increasing toward the outer surface. The variations in CEI composition across different depths suggest that the adsorption behavior of $DFOB^-$ and its preferential oxidation play a crucial role in interphase formation. According to previous studies, the B-containing decomposition products of DFOB preferentially degrade into small molecular and lightweight species such as BFC_2O_4, and BF_2CO_2 (see details in Figure S22).[28] These components exhibit a lower tendency to accumulate on the LCO surface compared to other inorganic components. In this case, their presence plays a key role in enhancing the densification of the CEI outer layer, thereby reinforcing its structural integrity and ensuring long-term stability.

The new CEI chemistries are clearly correlated with the different adsorption behavior of two electrolytes. Owing to the continuous decomposition of solvents in the solvation sheath of Li^+ in SE, an excessively thick CEI is formed with abundant organic components at the upper surface of LCO (Figure 3k). However, thanks to the inhibition of solvent participation by the presence of $DFOB^-$ in the inner-Helmholtz plane, both the organic components and the overall thickness of CEI decrease drastically in DE. The replacement of upper organic components by the boron-containing inorganic species from $DFOB^-$ anions constructs a compact, rigid and protective CEI that prevents persistent solvent decomposition as well as the degradation of the LCO at high voltages (Figure 3l). Therefore, the CEI components arising from solvent decomposition are replaced by boron-containing materials with higher ionic conductivity (Table S4). This leads to a significant reduction in interfacial impedance during the growth of the CEI, as demonstrated by the in situ EIS results (Figure S23).

The influence of different $DFOB^-$ ratios on CEI chemistry is further explored to explain the variation trend in electrochemical performance (Figure S3 and S4). FTIR and Raman spectroscopy are applied to analyze the bulk properties of the electrolytes (Figure S24). As the LiDFOB ratio increases, a weakening trend in the Li^+-EMC and Li^+-EC signals is observed, confirming that the introduction of $DFOB^-$ reduces Li^+-solvent interactions. However, when the LiDFOB concentration exceeds 0.5 M, the decline in electrochemical performance suggests that excessive $DFOB^-$ coordination with Li^+ is detrimental. Higher $DFOB^-$ concentrations lead to excessive decomposition, resulting in a thicker CEI compared to that formed at 0.5 M (Figure S25). Additionally, an excessive amount of $DFOB^-$ reduces the ionic conductivity of the bulk electrolyte (Figure S26), further impairing electrochemical performance.

High-Voltage Atabilities of $LiCoO_2$

An enhanced CEI can serve as a protective layer to stabilize the interfacial structural integrity of LCO especially at high potential ranges. A series of in situ/operando characterizations are further performed to monitor the real-time interfacial structural changes. Differential electrochemical mass spectrum (DEMS) detects the O_2 gas release from LCO during the charging process up to 4.7 V. The signal of O_2 is already prominent in SE at ~4.15 V (Figure 4a), while it is essentially absent in DE (Figure 4b). The enhanced stability of lattice oxygen implies a more stable chemical environment for the Co atoms on the lattice of LCO, which is confirmed by the in situ ultraviolet – visible (UV/Vis) spectroscopy (Figure 4c and 4d): during the charging process, the absorption peak intensity of dissolved Co at ~490 nm[29] in DE is one-third of that in SE when charging to 4.7 V. Furthermore, the irreversible O–Co–O deforma-

© 2025 Wiley-VCH GmbH

15213773, 0, Downloaded from https://onlinelibrary.wiley.com/doi/10.1002/anie.202425535 by University Town Of Shenzhen, Wiley Online Library on [17/03/2025]. See the Terms and Conditions (https://onlinelibrary.wiley.com/terms-and-conditions) on Wiley Online Library for rules of use; OA articles are governed by the applicable Creative Commons License

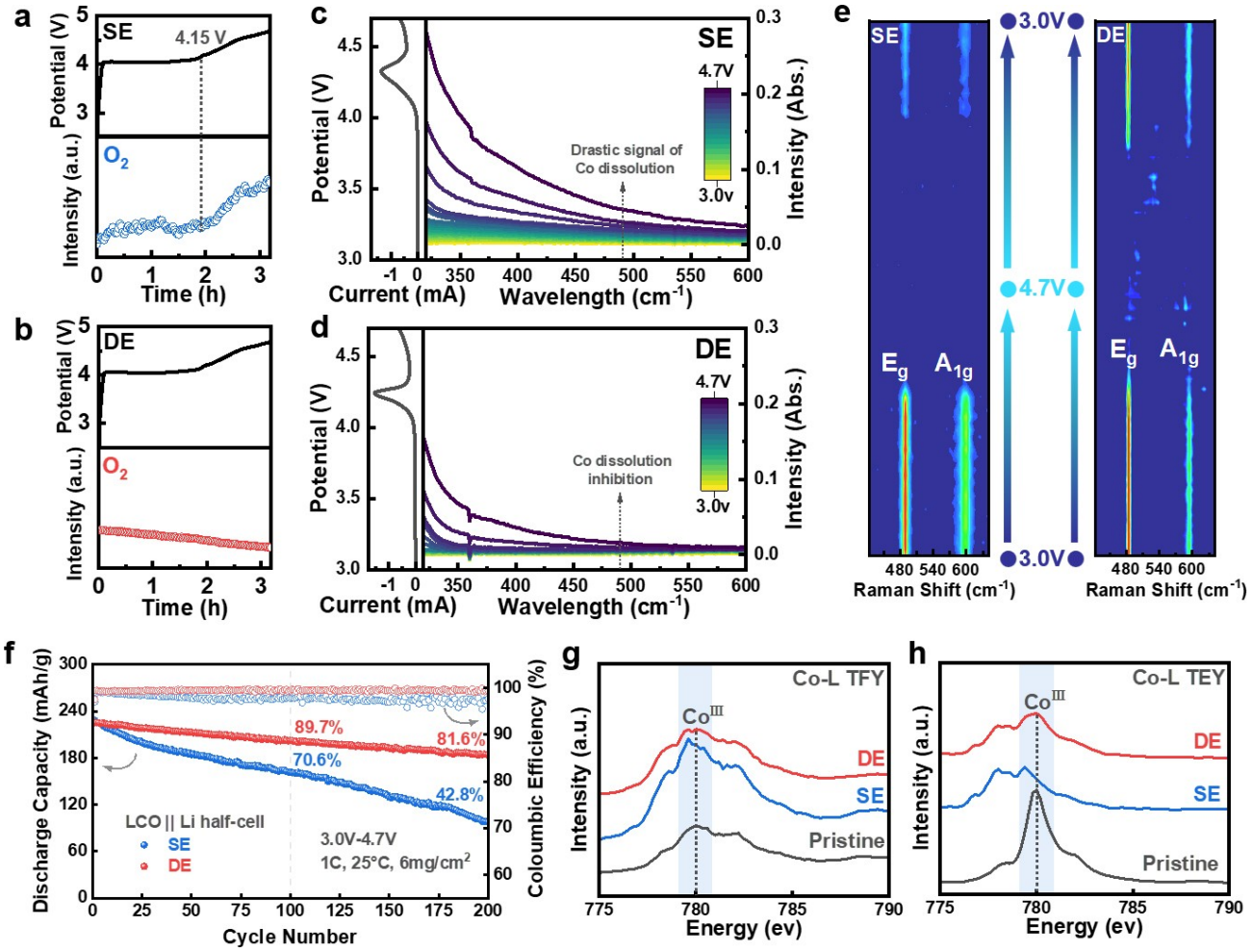

Figure 4. LCO stabilities at high voltage. Voltage profiles of LCO during charging and the corresponding O_2 release detection measured via DEMS in SE (a) and DE (b). In situ UV/Vis results of LCO cathode during charging in SE (c) and DE (d). (e) In situ Raman patterns of LCO during the first cycle in SE and DE. (f) Cycling performance comparisons at cut-off voltage of 4.7 V. sXAS under the mode of total fluorescence yield (g) and total electron yield (h) of Co L_2 and L_3 edges of LCO before and after cycling in both electrolytes.

tion (Eg) and Co–O symmetric stretching (A1 g)[9a] peaks in in situ confocal Raman spectra (Figure 4e, Figure S27) also indicate incomplete re-lithiation[9a] and irreversible evolution of LCO structure in SE. By contrast, the signals of both O–Co–O and Co–O bonds of LCO cycled in DE can be recovered with relatively higher reversibility during lithiation. Therefore, it can be concluded that the CEI formed in DE inhibits the undesirable H1-3 phase change and prevents the irreversible structural transformation of LCO lattice near surface, which is further verified by in situ XRD (Figure S28).[29]

The improvement in structural maintenance at high potentials further enhances cycling stability and high performance during long-term cycling. Figure S29 and Figure 4f compare the long-term cycling performance of LCO in SE and DE under the rate of 1 C (200 mA g^{-1}) at a high cut-off potential of 4.6 V and 4.7 V, respectively, that DE demonstrates significantly improved capacity retention, Columbic efficiency and potential retention (Figure S30) compared to SE. At a higher temperature (45°C), the difference in high-voltage cycling stability between the two electrolytes becomes more pronounced (Figure S31). Therefore, we infer that the dissolution of the CEI formed by SE is a key reason for its failure. To verify this speculation, LCO was first cycled at 0.1 C, then let to rest for 20 hours, allowing sufficient time for the CEI to dissolve into the electrolytes (Figure S32). In SE, each resting period is accompanied by gradual potential decline and a drop in coulombic efficiency. This can be attributed to the re-exposure of the LCO surface caused by CEI dissolution, resulting in oxidation of electrolyte components by the charged LCO. In contrast, the CEI dissolution in DE is significantly inhibited, with neither potential decline during the rest period nor a decrease in coulombic efficiency after the rest period. The dissolution phenomenon can also be directly visualized in TEM images (Figure S33). In SE, a thicker and more uneven CEI morphology is observed after the initial cycle, along with drastic morphological changes due to dissolution. In contrast, the CEI formed in DE consistently maintains a compact and uniform morphology,

© 2025 Wiley-VCH GmbH

15213773, 0, Downloaded from https://onlinelibrary.wiley.com/doi/10.1002/anie.202425535 by University Town Of Shenzhen, Wiley Online Library on [17/03/2025]. See the Terms and Conditions (https://onlinelibrary.wiley.com/terms-and-conditions) on Wiley Online Library for rules of use; OA articles are governed by the applicable Creative Commons License

indicating superior stability, which aligns well with the TEM observations of cycled LCO (Figure 3a-b). To evaluate the above performance improvements induced by $DFOB^-$ in commercial batteries, LCO||graphite pouch cells were assembled and tested (Figure S34). The cells delivered superior capacity retention of 86.3 % after 1000 cycles with average coulombic efficiency of 99.95 %. To elucidate the coupling effects of LiDFOB on Li anode in half-cells, cycling tests were conducted in Li||Li symmetric cells (Figure S35), where no significant performance difference between SE and DE can be observed after cycling for 120 hours. This result indicates that the performance improvement is mainly attributed to the cathode side.

The failure mechanisms of LCO after cycling are further investigated using synchrotron soft X-ray absorption spectroscopy (sXAS) of Co L_2- and L_3-edge. Under the mode of both total fluorescence yield (TFY, Figure 4g) and total electron yield (TEY, Figure 4h), a more obvious shift of the Co^{3+} peak to the lower energy after 400 cycles can be observed in SE than that in DE, which is attributed to the reduction of Co^{3+} to Co^{2+} induced by electrolyte oxidation accompanied with the oxygen loss and irreversible phase transformation.[2a] The chemical states and local coordination environment of the Co element are investigated via hard XAS at the Co K-edge. X-ray absorption near edge structure (XANES) demonstrates that compared to DE, the valence state of cobalt in LCO cycled in SE decreased after 100 cycles (Figure S36a). In addition, extended X-ray absorption fine structure (EXAFS) reveals that the LCO cycled in DE maintains more intact local coordination environment of Co than that in SE (Figure S36b). High-resolution transmission electron microscope (HRTEM) images (Figure S37) further support this observation, where an obvious rock salt phase transformation can be detected near the surface of LCO recovered from SE. Raman spectra of LCO cycled in DE also show sharper Eg and A1 g signals than that in SE (Figure S38), which can be attributed to the improved interfacial and structural stability of LCO in DE. XRD crystallography refinement data also show that the lattice changes in the crystal structure of LCO cycled in DE are less pronounced compared to those in SE (Figure S39, Table S5 and S6).

Conclusions

In summary, we systematically investigated the adsorptive behavior of different anions on the LCO cathode surface and monitored the subsequent interfacial structures and the eventual interphasial chemistries. We discovered that partially replacing PF_6^- anion with $DFOB^-$ results in the reconstruction of a more inorganic CEI that stabilizes LCO reversibility at high voltages. Combining multiple in situ interfacial characterization techniques, we successfully described the molecular-level picture of how an anion adsorption mediates the CEI formation process: the preferential adsorption of anions on the LCO surface is found to effectively inhibit the aggregation of solvents at the interface, forming a CEI dominated by anion-derived species. Owing to the new CEI chemistry, the structural stability of LCO can be well maintained during high-voltage operations, exhibiting a high reversible capacity and drastically enhanced capacity retention. This new knowledge correlating interfacial structure and interphasial chemistry with firm in situ/operando experimental evidences not only helps us to fully understand the convoluted process of CEI formation, but also provides guidelines in designing new electrolytes and interphases for future battery chemistries.

Acknowledgements

F.P. and L.Y. thank the financial support by Shenzhen Science and Technology Research Grant (No. ZDSYS201707281026184, JSGG20220831095604008) and Soft Science Research Project of Guangdong Province (2017B030301013). L.Y. acknowledges financial support from National Natural Science Foundation of China (No. 52303263). The authors thank Shanghai Synchrotron Radiation Facility (SSRF) (beamline 02B02) for the allocation of synchrotron beam time, and the Anhui Absorption Spectroscopy Analysis Instrument Co, Ltd. for XAFS measurements and analysis.

Conflict of Interest

The authors declare that they have no known competing financial interests or personal relationships that could have appeared to influence the work reported in this paper.

Data Availability Statement

The data that support the findings of this study are available from the corresponding author upon reasonable request.

Keywords: cathode electrolyte interphase · interface adsorption · inner Helmholtz plane · in situ interface characterization · high voltage battery

[1] a) W. Huang, L. Yang, Z. Chen, T. Liu, G. Ren, P. Shan, B. W. Zhang, S. Chen, S. Li, J. Li, C. Lin, W. Zhao, J. Qiu, J. Fang, M. Zhang, C. Dong, F. Li, Y. Yang, C. J. Sun, Y. Ren, Q. Huang, G. Hou, S. X. Dou, J. Lu, K. Amine, F. Pan, *Adv. Mater.* **2022**, *34*, e2202745; b) L. Yang, K. Yang, J. Zheng, K. Xu, K. Amine, F. Pan, *Chem. Soc. Rev.* **2020**, *49*, 4667–4680.

[2] a) M. Cai, Y. Dong, M. Xie, W. Dong, C. Dong, P. Dai, H. Zhang, X. Wang, X. Sun, S. Zhang, M. Yoon, H. Xu, Y. Ge, J. Li, F. Huang, *Nat. Energy* **2023**, *8*, 159–168; b) X. Yang, C. Wang, P. Yan, T. Jiao, J. Hao, Y. Jiang, F. Ren, W. Zhang, J. Zheng, Y. Cheng, X. Wang, W. Yang, J. Zhu, S. Pan, M. Lin, L. Zeng, Z. Gong, J. Li, Y. Yang, *Adv. Energy Mater.* **2022**, *12*, 2200197; c) Y. Yan, S. Weng, A. Fu, H. Zhang, J. Chen, Q. Zheng, B. Zhang, S. Zhou, H. Yan, C.-W. Wang, Y. Tang, H. Luo, B.-W. Mao, J. Zheng, X. Wang, Y. Qiao, Y. Yang, S.-G. Sun, *ACS Energy Lett.* **2022**, *7*, 2677–2684; d) C. Lin, J. Li, Z. W. Yin, W. Huang, Q. Zhao, Q. Weng, Q. Liu, J. Sun, G. Chen, F. Pan, *Adv. Mater.* **2024**, *36*, e2307404.

© 2025 Wiley-VCH GmbH

15213773, 0, Downloaded from https://onlinelibrary.wiley.com/doi/10.1002/anie.202425535 by University Town Of Shenzhen, Wiley Online Library on [17/03/2025]. See the Terms and Conditions (https://onlinelibrary.wiley.com/terms-and-conditions) on Wiley Online Library for rules of use; OA articles are governed by the applicable Creative Commons License

[3] a) X. Fan, C. Wang, *Chem. Soc. Rev.* **2021**, *50*, 10486–10566; b) N. Dupré, J. F. Martin, J. Oliveri, P. Soudan, D. Guyomard, A. Yamada, R. Kanno, *J. Electrochem. Soc.* **2009**, *156*, C180–C185; c) T. Kim, L. K. Ono, Y. Qi, *J. Mater. Chem. A* **2023**, *11*, 221–231; d) T. U. Wi, C. Park, S. Ko, T. Kim, A. Choi, V. Muralidharan, M. Choi, H. W. Lee, *Nano Lett.* **2024**, *24*, 7783–7791.

[4] a) J. Xiao, *Science* **2022**, *376*, 455–456; b) J. Xiao, F. Shi, T. Glossmann, C. Burnett, Z. Liu, *Nat. Energy* **2023**, *8*, 329–339.

[5] a) J. Zhang, P.-F. Wang, P. Bai, H. Wan, S. Liu, S. Hou, X. Pu, J. Xia, W. Zhang, Z. Wang, B. Nan, X. Zhang, J. Xu, C. Wang, *Adv. Mater.* **2022**, *34*, 2108353; b) J. Liu, M. Wu, X. Li, D. Wu, H. Wang, J. Huang, J. Ma, *Adv. Energy Mater.* **2023**, *13*, 2300084.

[6] a) W. Zuo, M. Luo, X. Liu, J. Wu, H. Liu, J. Li, M. Winter, R. Fu, W. Yang, Y. Yang, *Energy Environ. Sci.* **2020**, *13*, 4450–4497; b) S. Venkatraman, Y. Shin, A. Manthiram, *Electrochem. Solid-State Lett.* **2003**, *6*, A9–A12; c) W. S. Yoon, K. B. Kim, M. G. Kim, M. K. Lee, H. J. Shin, J. M. Lee, J. S. Lee, C. H. Yo, *J. Phys. Chem. B* **2002**, *106*, 2526–2532.

[7] a) J. Li, C. Lin, M. Weng, Y. Qiu, P. Chen, K. Yang, W. Huang, Y. Hong, J. Li, M. Zhang, C. Dong, W. Zhao, Z. Xu, X. Wang, K. Xu, J. Sun, F. Pan, *Nat. Nanotechnol.* **2021**, *16*, 599–605; b) P. Liu, L. Yang, B. Xiao, H. Wang, L. Li, S. Ye, Y. Li, X. Ren, X. Ouyang, J. Hu, F. Pan, Q. Zhang, J. Liu, *Adv. Funct. Mater.* **2022**, *32*, 2208586.

[8] a) J. Zhang, P. F. Wang, P. Bai, H. Wan, S. Liu, S. Hou, X. Pu, J. Xia, W. Zhang, Z. Wang, B. Nan, X. Zhang, J. Xu, C. Wang, *Adv. Mater.* **2022**, *34*, e2108353; b) J. Liu, B. Yuan, N. He, L. Dong, D. Chen, S. Zhong, Y. Ji, J. Han, C. Yang, Y. Liu, W. He, *Energy Environ. Sci.* **2023**, *16*, 1024–1034; c) X. Min, C. Han, S. Zhang, J. Ma, N. Hu, J. Li, X. Du, B. Xie, H. J. Lin, C. Y. Kuo, C. T. Chen, Z. Hu, L. Qiao, Z. Cui, G. Xu, G. Cui, *Angew. Chem. Int. Ed.* **2023**, *62*, e202302664; d) C. Yang, X. Liao, X. Zhou, C. Sun, R. Qu, J. Han, Y. Zhao, L. Wang, Y. You, J. Lu, *Adv. Mater.* **2023**, *35*, e2210966; e) W. Xue, R. Gao, Z. Shi, X. Xiao, W. Zhang, Y. Zhang, Y. G. Zhu, I. Waluyo, Y. Li, M. R. Hill, Z. Zhu, S. Li, O. Kuznetsov, Y. Zhang, W.-K. Lee, A. Hunt, A. Harutyunyan, Y. Shao-Horn, J. A. Johnson, J. Li, *Energy Environ. Sci.* **2021**, *14*, 6030–6040.

[9] a) F. C. Zhang, N. Qin, Y. Z. Li, H. Guo, Q. M. Gan, C. Zeng, Z. Q. Li, Z. Y. Wang, R. Wang, G. Y. Liu, S. Gu, H. Huang, Z. L. Yang, J. Wang, Y. H. Deng, Z. G. Lu, *Energy Environ. Sci.* **2023**, *16*, 4345–4355; b) Y. Qin, K. Xu, Q. Wang, M. Ge, T. Cheng, M. Liu, H. Cheng, Y. Hu, C. Shen, D. Wang, Y. Liu, B. Guo, *Nano Energy* **2022**, *96*, 107082.

[10] a) H. Zhang, Z. Zeng, R. He, Y. Wu, W. Hu, S. Lei, M. Liu, S. Cheng, J. Xie, *Energy Storage Mater.* **2022**, *48*, 393–402; b) X. Ren, X. Zhang, Z. Shadike, L. Zou, H. Jia, X. Cao, M. H. Engelhard, B. E. Matthews, C. Wang, B. W. Arey, X.-Q. Yang, J. Liu, J.-G. Zhang, W. Xu, *Adv. Mater.* **2020**, *32*, 2004898.

[11] J. Hu, Y. Ji, G. Zheng, W. Huang, Y. Lin, L. Yang, F. Pan, *Aggregate* **2022**, *3*, e153.

[12] Y. Ji, J. Qiu, W. Zhao, T. Liu, Z. Dong, K. Yang, G. Zheng, G. Qian, M. Yang, Q. Chen, K. Amine, F. Pan, L. Yang, *Chem* **2023**, *9*, 2943–2955.

[13] a) P. Bai, X. Ji, J. Zhang, W. Zhang, S. Hou, H. Su, M. Li, T. Deng, L. Cao, S. Liu, X. He, Y. Xu, C. Wang, *Angew. Chem. Int. Ed.* **2022**, *61*, e202202731; b) K. Guo, C. Zhu, H. Wang, S. Qi, J. Huang, D. Wu, J. Ma, *Adv. Energy Mater.* **2023**, *13*, 2204272.

[14] K. Xu, A. von Wald Cresce, *J. Mater. Res.* **2012**, *27*, 2327–2341.

[15] K. Xu, *Electrolytes, Interfaces and Interphases, RSC Press* **2023**.

[16] A. von Wald Cresce, M. Gobet, O. Borodin, J. Peng, S. M. Russell, E. Wikner, A. Fu, L. Hu, H.-S. Lee, Z. Zhang, X.-Q. Yang, S. Greenbaum, K. Amine, K. Xu, *J. Phys. Chem. C* **2015**, *119*, 27255–27264.

[17] a) M. Mao, B. Huang, Q. Li, C. Wang, Y.-B. He, F. Kang, *Nano Energy* **2020**, *78*, 105282; b) J. Zheng, M. H. Engelhard, D. Mei, S. Jiao, B. J. Polzin, J.-G. Zhang, W. Xu, *Nat. Energy* **2017**, *2*, 17012.

[18] K. Mizushima, P. C. Jones, P. J. Wiseman, J. B. Goodenough, *Mater. Res. Bull.* **1980**, *15*, 783–789.

[19] L. Yu, H. Liu, Y. Wang, N. Kuwata, M. Osawa, J. Kawamura, S. Ye, *Angew. Chem. Int. Ed.* **2013**, *52*, 5753–5756.

[20] a) S. H. Lee, H. L. Lee, H. J. Youn, *Cellulose* **2014**, *21*, 1251–1260; b) H. A. Huellemeier, N. M. Eren, J. Ortega-Anaya, R. Jimenez-Flores, D. R. Heldman, *Chem. Eng. J.* **2022**, *247*, 117004; c) A. D. Easley, T. Ma, C. I. Eneh, J. Yun, R. M. Thakur, J. L. Lutkenhaus, *J. Polym. Sci.* **2021**, *60*, 1090–1107; d) N.-J. Cho, C. W. Frank, B. Kasemo, F. Höök, *Nat. Protoc.* **2010**, *5*, 1096–1106.

[21] N. Shpigel, M. D. Levi, D. Aurbach, *Energy Storage Mater.* **2019**, *21*, 399–413.

[22] a) V. Dargel, N. Shpigel, S. Sigalov, P. Nayak, M. D. Levis, L. Daikhin, D. Aurbach, *Nat. Commun.* **2017**, *8*, 1389; b) N. Shpigel, M. D. Levi, S. Sigalov, O. Girshevitz, D. Aurbach, L. Daikhin, P. Pikma, M. Marandi, A. Jänes, E. Lust, N. Jäckel, V. Presser, *Nat. Mater.* **2016**, *15*, 570–575.

[23] a) Z. Yang, B. J. Ingram, L. Trahey, *J. Electrochem. Soc.* **2014**, *161*, A1127–A1131; b) Z. Yang, A. A. Gewirth, L. Trahey, *ACS Appl. Mater. Interfaces* **2015**, *7*, 6557–6566; c) A. A. Hubaud, Z. Yang, D. J. Schroeder, F. Dogan, L. Trahey, J. T. Vaughey, *J. Power Sources* **2015**, *282*, 639–644.

[24] Y. Zou, Z. Ma, G. Liu, Q. Li, D. Yin, X. Shi, Z. Cao, Z. Tian, H. Kim, Y. Guo, C. Sun, L. Cavallo, L. Wang, H. N. Alshareef, Y. K. Sun, J. Ming, *Angew. Chem. Int. Ed.* **2023**, *62*, e202216189.

[25] a) M.-Y. Zhou, X.-Q. Ding, J.-F. Ding, L.-P. Hou, P. Shi, J. Xie, B.-Q. Li, J.-Q. Huang, X.-Q. Zhang, Q. Zhang, *Joule* **2022**, *6*, 2122–2137; b) Z. Yu, H. Wang, X. Kong, W. Huang, Y. Tsao, D. G. Mackanic, K. Wang, X. Wang, W. Huang, S. Choudhury, Y. Zheng, C. V. Amanchukwu, S. T. Hung, Y. Ma, E. G. Lomeli, J. Qin, Y. Cui, Z. Bao, *Nat. Energy* **2020**, *5*, 526–533.

[26] M. Matsui, S. Deguchi, H. Kuwata, N. Imanishi, *Electrochemistry* **2015**, *83*, 874–878.

[27] Z. Yang, M. C. Dixon, R. A. Erck, L. Trahey, *ACS Appl. Mater. Interfaces* **2015**, *7*, 26585–26594.

[28] a) S. Shui Zhang, *Electrochem. Commun.* **2006**, *8*, 1423–1428; b) O. Ka, F. Cheng, L. Wen, X. Wang, T. Wang, X. Zeng, W. Lu, L. Dai, *J. Mater. Chem. A* **2024**, *12*, 11487–11501; c) M. H. Fu, K. L. Huang, S. Q. Liu, J. S. Liu, Y. K. Li, *J. Power Sources* **2010**, *195*, 862–866; d) Y. Zhu, Y. Li, M. Bettge, D. P. Abraham, *J. Electrochem. Soc.* **2012**, *159*, A2109–A2117; e) M. Mao, X. Ji, Q. Wang, Z. Lin, M. Li, T. Liu, C. Wang, Y. S. Hu, H. Li, X. Huang, L. Chen, L. Suo, *Nat. Commun.* **2023**, *14*, 1082.

[29] J.-N. Zhang, Q. Li, C. Ouyang, X. Yu, M. Ge, X. Huang, E. Hu, C. Ma, S. Li, R. Xiao, W. Yang, Y. Chu, Y. Liu, H. Yu, X.-Q. Yang, X. Huang, L. Chen, H. Li, *Nat. Energy* **2019**, *4*, 594–603.

Manuscript received: December 29, 2024
Accepted manuscript online: February 26, 2025
Version of record online: ■■, ■■

© 2025 Wiley-VCH GmbH

15213773, 0, Downloaded from https://onlinelibrary.wiley.com/doi/10.1002/anie.202425535 by University Town Of Shenzhen, Wiley Online Library on [17/03/2025]. See the Terms and Conditions (https://onlinelibrary.wiley.com/terms-and-conditions) on Wiley Online Library for rules of use; OA articles are governed by the applicable Creative Commons License

Research Article

Batteries

Y. Ji, Y. Huang, Z. Dong, J. Fang, P. Liu, S. Liu, A. Cao, H. Xue, S. Chen, J. Qiu, P.-H. Du, K. Xie, S. Xue, T. Shen, G. Zheng, X. Zhao, Z.-W. Yin, K. Yang, H. Lin, K. Xu,* F. Pan,* L. Yang* **e202425535**

Anion Adsorption at the Inner-Helmholtz Plane Directs Cathode Electrolyte Interphase Formation

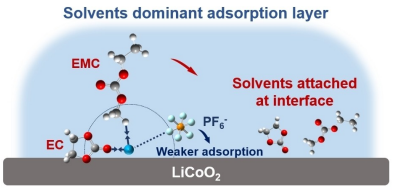

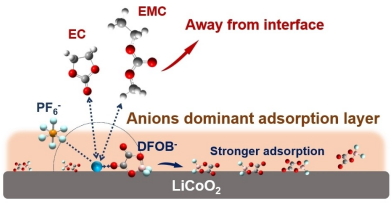

The role of anion adsorption at the inner-Helmholtz plane in directing CEI formation was investigated using multiple in situ/operando techniques. QCM–D directly observes its influence on interfacial structure, while in situ spectroscopy and EQCM–D confirm its impact on CEI chemistry. The anion-driven interphase leads to a more inorganic-rich CEI, suppressing electrolyte decomposition and enhancing $LiCoO_2$ cycling stability at high voltages.

© 2025 Wiley-VCH GmbH

15213773, 0, Downloaded from https://onlinelibrary.wiley.com/doi/10.1002/anie.202425535 by University Town Of Shenzhen, Wiley Online Library on [17/03/2025]. See the Terms and Conditions (https://onlinelibrary.wiley.com/terms-and-conditions) on Wiley Online Library for rules of use; OA articles are governed by the applicable Creative Commons License